Human Atlas of the Cardiac Fiber Architecture: Study on a Healthy Population

Herve Lombaert, Jean-Marc Peyrat, Pierre Croisille, Stanislas Rapacchi, Laurent Fanton, Farida Cheriet, Patrick Clarysse, Isabelle Magnin, Hervé Delingette, Nicholas Ayache

***Abstract*—Cardiac fibers, as well as their local arrangement in laminar sheets, have a complex spatial variation of their orientation that has an important role in mechanical and electrical cardiac functions. In this paper, a statistical atlas of this cardiac fiber architecture is built for the first time using human datasets. This atlas provides an average description of the human cardiac fiber architecture along with its variability within the population. In this study, the population is composed of 10 healthy human hearts whose cardiac fiber architecture is imaged *ex vivo* with DT-MRI acquisitions. The atlas construction is based on a computational framework that minimizes user interactions and combines most recent advances in image analysis: Graph Cuts for segmentation, Symmetric Log-domain Diffeomorphic Demons for registration, and Log-Euclidean metric for diffusion tensor processing and statistical analysis. Results show that the helix angle of the average fiber orientation is highly correlated to the transmural depth and ranges from -41° on the epicardium to $+66^\circ$ on the endocardium. Moreover, we find that the fiber orientation dispersion across the population ($\pm 13^\circ$) is lower than for the laminar sheets ($\pm 31^\circ$). This study, based on human hearts, extends previous studies on other mammals with concurring conclusions and provides a description of the cardiac fiber architecture more specific to human and better suited for clinical applications. Indeed, this statistical atlas can help to improve the computational models used for radiofrequency ablation (RFA), cardiac resynchronization therapy (CRT), surgical ventricular restoration, or diagnosis and follow-ups of heart diseases due to fiber architecture anomalies.**

***Index Terms*—Diffusion weighted imaging, Heart, Atlases**

I. Introduction

CARDIOVASCULAR disease is a leading cause of death in developing countries. The understanding of the cardiac muscle structure and functions is essential for the diagnosis and the treatment of many heart pathologies. The cardiac fiber architecture, a complex organization of the myocardium fibers [45], [28], determines various cardiac mechanical functions [10], cardiac electrophysiology patterns [24], and remodeling processes [53]. The assessment of structural variability is important for a better understanding of the human heart physiology [8], [9] and for a more accurate modeling of the heart. Such models with a complete description of the fiber architecture can be used for clinical applications. For instance, the planning of radiofrequency ablation (RFA) [40] or cardiac resynchronization therapy (CRT) [44], with respectively the localization of the zone to ablate and the positioning of the pacing electrodes, can be optimized using electro-mechanical models of the heart whose fiber structure is a key information for more accurate simulations and predictions.

The fibrous nature of the heart has been known for centuries, Harvey reported as early as 1628 in *De Motu Cordis* [18] the functional role of the cardiac fibers. In the modern era, Streeter [45] suggested that the cardiac fibers are organized as nested surfaces. Further studies on the cardiac fiber architecture also revealed common features among species [6]. The fibers, locally organized as laminar sheets, appear to be consistently structured as two counter wound spirals wrapping around the heart clockwise on the epicardial surface and counterclockwise on the endocardial surface [45], [28]. The helical myocardial band of Torrent-Guasp [47] is another model (triggering controversial discussions [52]) that hypothesizes the existence of a single muscular band folding onto itself to form the whole heart. Nevertheless, cardiac fiber studies mainly focus on the local orientation of fibers with their angle on the tangent plane and on the horizontally normal plane of the epicardium called respectively the helix and the transverse angles. In humans, the variability of the cardiac fiber architecture was studied using tedious work on histological slices [16], and thus hard to assess completely in 3D. So far, more detailed cardiac fiber architecture has been mainly speculated from studies on other species [33].

The cardiac fiber architecture of single human hearts have already been visualized and studied using DT-MRI [55], [41], [43]. However, due to an extreme rarity of healthy human hearts (they are rather transplanted than used for research), no statistical study has yet been performed on humans. With an access to a unique post-mortem human dataset [12], [13], [39], the presented work aimed at building, for the first time, a statistical atlas of the human cardiac fiber architecture from 10 healthy *ex vivo* hearts imaged with DT-MRI. This work is an extended version of preliminary results [29]. Here, the method is fully explained and we provide an extensive statistical study on the fiber variability as well as a refined analysis of the transmural distribution of the fiber helix and transverse angle.

Manuscript received November 11st, 2011; Revised March 23rd, 2012. This work was supported by the National Science and Engineering Research Council of Canada (NSERC), the Michael Smith Scholarship (CGS-MSFSS), and the EGIDE/INRIA Scholarship.

H. Lombaert is a visiting student at INRIA, Asclepios project-team, Sophia-Antipolis, France and with École Polytechnique de Montréal, Canada

J.-M. Peyrat is with Siemens Molecular Imaging, Oxford, UK

P. Croisille, S. Rapacchi, P. Clarysse and I. Magnin are with CREATIS, Université de Lyon, France

F. Cheriet is with École Polytechnique de Montréal, Canada

L. Fanton is with Institut Universitaire de Médecine Légale, Université de Lyon, France

H. Delingette and N. Ayache are with INRIA, Asclepios project-team, Sophia-Antipolis, France

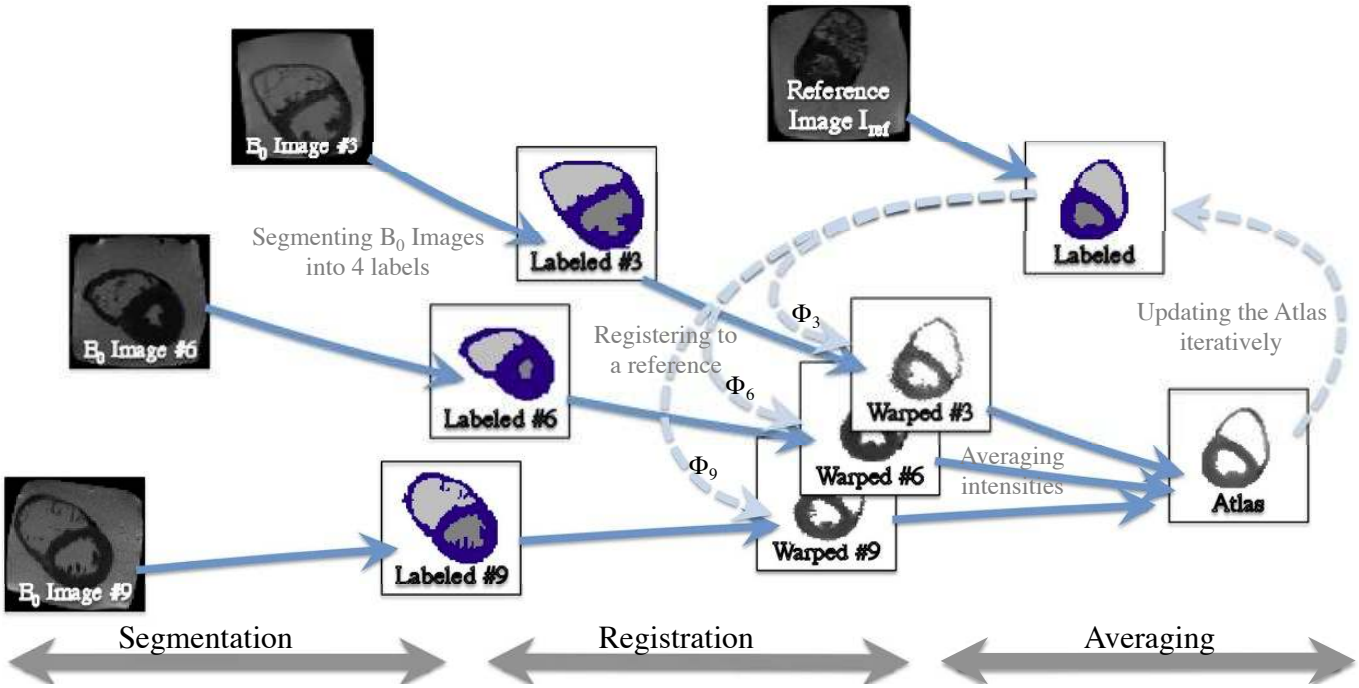

Fig. 1. *Construction of the morphological atlas*: From the acquired images, the myocardium and the blood masses are segmented as described in Section II-B1. The images are then aligned and deformed toward a reference image. The registration is performed using Non-rigid Symmetric Diffeomorphic Log-Demons as explained in Section II-B2. The atlas is constructed iteratively by averaging acquired images in the average shape of the atlas as explained in Section II-B3.

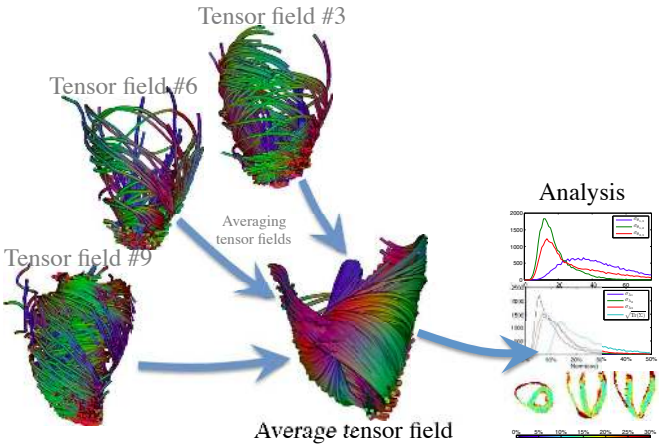

Fig. 2. *Construction of the statistical atlas* of the human cardiac fiber architecture. All acquired tensors are warped using the transformation found during the construction of the morphological atlas. With the average tensor and its covariance matrix, the statistical analysis is carried on. The tensor field illustrations show tractographies generated with MedINRIA.

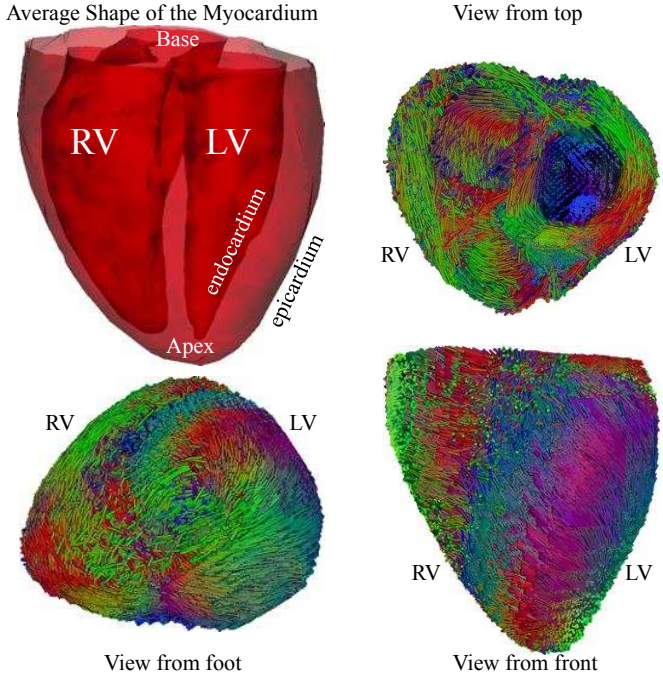

Fig. 3. *Average geometry and fiber orientations* with *(upper left)* the average shape of the myocardium, *(upper right)* short axial view from top, *(lower left)* apical view from foot, *(lower right)* long axial view from front. The *r,g,b* color of the tracked fibers indicates the *x,y,z* components of the local orientation of the fiber.

The atlas construction and the population variability study are performed using a refined version of the computational framework proposed by Peyrat *et al.* [38]. The method has been automated and adapted to process the available images, which are at a lower resolution than in [38]. It is described in details for reproducibility and can easily be reused for studies that includes a large number of hearts. Firstly, we present the strategy for the construction of the atlas eased by the use of a more recent registration method, the Symmetric Log-demons [50], [32]. The registration is also guided by a segmentation step involving minimal user interaction using Graph Cuts [5] to cope with topological issues that could occur with a basic thresholding on images with lower resolution than in [38]. Secondly, we use the same statistical framework on diffusion tensors as in [38] to analyze the variability of the fiber architecture. Thirdly, we present the main contribution: the

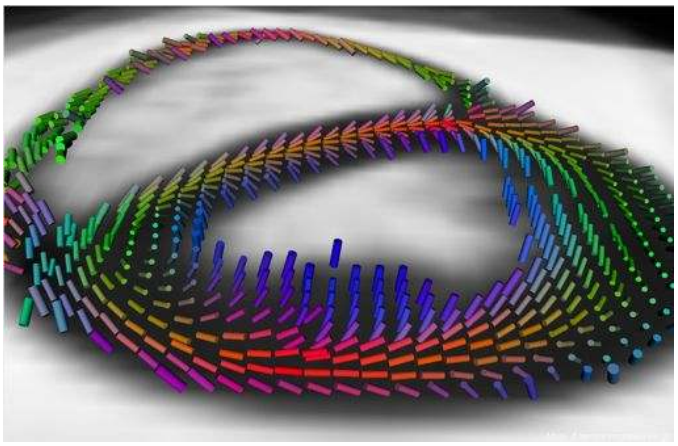

Fig. 4. *Average fiber orientation* seen on a short axis slice. The left ventricle is on the foreground and the right ventricle on the background. The cylinders indicates the direction of the first eigenvector in the average diffusion tensor field. Color indicates the local orientation of the fiber. The transmural variation is visible in the left ventricle and in the midwall. The vertical papillary muscles are visible in darker blue.

provision and analysis of a human statistical atlas, performed both globally over the whole myocardium and locally within several myocardial segments. Common features of the cardiac fiber architecture along their variabilities are shown for the first time in a population of healthy human subjects. Finally, we discuss possible improvements of our method and give perspectives on our results.

II. Material and Method

The dataset and its acquisition protocol, consisting of anatomical $b = 0$ images and their associated DT-MRI tensor fields, is first presented. The transverse anisotropy in each tensor field provides confidence for the presence of a secondary fiber structure (i.e., the laminar sheet). The method constructing the DT-MRI atlas is described with the semi-automatic segmentation of the myocardium followed by the fully automatic groupwise registration of the anatomical images (Fig. 1), and with thereafter the warping of the tensor fields (Fig. 2). Finally, the statistical framework on diffusion tensors is explained. It provides an average representation (Fig. 3 and 4) of the cardiac fiber architecture as well as its variability in terms of fiber and laminar sheet orientations.

A. Data Acquisition

The hearts were explanted within 24 hours after death and *ex vivo* imaging was performed without any additional delay. The hearts did not exhibit any patent contracture compared to what is commonly observed in organs of more than a few days after death. Special care was taken to carefully remove any remaining blood or mural thrombi by flushing the ventricles with an isotonic solution. The ventricles were then filled with an hydrophilic and isotonic gel to remove any air and to restore a normal anatomic configuration. Finally, the hearts were placed in a plastic container filled with the same hydrophilic gel. The posterior wall of the atria were partially removed to give access to the atria-ventricular valves. The preparation and handling of the hearts were established with forensic specialists to avoid any additional delay and any potential changes to the common forensic procedure that was performed after imaging on the fresh non-fixed entire hearts.

Each heart with its plastic container was placed in a 16 element head coil and was imaged with a 1.5T MR scanner (Avanto Siemens). The main MRI parameters of the diffusion weighted EPI sequence (bipolar scheme) are: $\mathrm{TE/TR} = 69/6500$ ms, 6 excitations (with polarity alternation), voxels of $2\times2\times2$ mm^3, parallel imaging (GRAPPA with acceleration factor 2), partial Fourier (6/8), base resolution matrix of 128, $\mathrm{BW} = 1628$ Hz/Px, echo spacing of 0.7 ms, 12 directions, and $b = 1000$ s.mm^2 with a $\mathrm{PSNR} = 16.44$ dB. The acquisition protocol is detailed in [12], [13]. The b=0 images along their myocardial masks and illustrative fiber tractographies (generated using a spin glass model [11]) are shown on Fig. 5.

DT-MRI measures the local spatial diffusion within one voxel. The maximal local direction of diffusion, revealed by the primary eigenvector $\mathbf{v}_1$ of the diffusion tensor matrix D, occurs along the main structure, i.e., the fiber, while the secondary eigenvector, $\mathbf{v}_2$, is assumed to lay within the laminar sheet. The tertiary eigenvector, $\mathbf{v}_3$, would thus be related to the normal of the laminar sheet (illustrated in Fig. 6(a)). Although strong evidences exist toward this assumption [22], [23], [42], [49], we first need to ensure that pairs of eigenvectors and eigenvalues are distinguishable and hold meaningful structural information. The corresponding null hypothesis would imply transverse isotropy (i.e., equal secondary and tertiary eigenvalues $d_2 = d_3$). Rejecting it, by observing a transverse anisotropy, would give an indication that a secondary structure exists in the transverse plane of the primary eigenvector. We do so by showing that the eigenvalues are not equal and that the eigenvectors are locally structured.

Since $d_2 > d_3 > 0$, the ratio d_3/d_2 is defined between 0 and 1 and the mode of the ratio distribution should be close to one in case of transverse isotropy. The figure 7 shows that even though the distributions of the eigenvalues are very close, the peak of the ratio distribution d_3/d_2 is at 0.86 and suggests that the secondary and the tertiary eigenvalues are not equal. Furthermore, Helm *et al.* [23], [21] explain that in case of transverse isotropy the secondary and tertiary eigenvectors should rotate randomly around the principal axis of diffusion. They reject this null hypothesis with a Kolmogorov-Smirnov (K-S) test where the local distribution of the angle $\alpha = \cos^{-1}(|\mathbf{v}_2 \cdot \mathbf{v}_n|)$, between the secondary eigenvector $\mathbf{v}_2$ and a local reference vector $\mathbf{v}_n$ defined in each myocardial segment, is not uniform (i.e., testing if α is randomly distributed, or not, on the transverse plane). The local reference, $\mathbf{v}_n$, is fixed and is chosen to be the best orthogonal vector to the set of first eigenvectors within each AHA segment. Furthermore, the maximal distance between the cumulative distribution $F_\alpha(\theta)$ of the angle α and the cumulative distribution θ/π of the uniform distribution gives a measure of confidence with the R-value: $R = \max_{\theta=[0,2\pi]}\{|\theta/\pi - F_\alpha(\theta)|\}$ (see [23], [21] for more details). The critical R-value $R_c = 0.06$ is chosen [21] using the average number of pixels in each AHA segment (1247 pixels), i.e., if $R > R_c$, the distribution of the angle α can be considered non-uniform. The table II shows for all

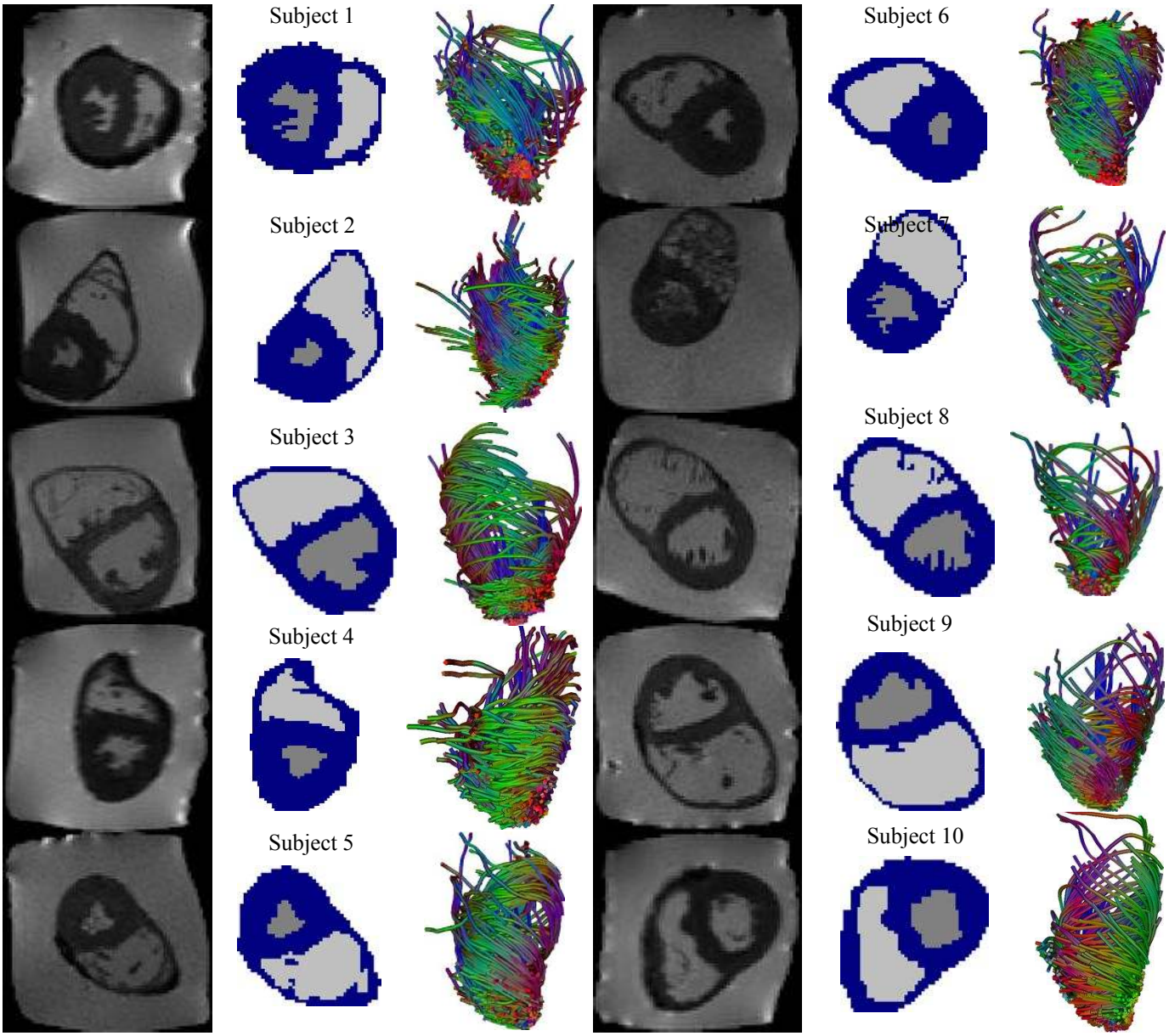

Fig. 5. *Dataset* consisting of 10 healthy *ex vivo* human hearts. On the left, the b=0 images acquired in the DTI studies. In the middle, segmented myocardium (in blue) with left (in dark gray) and right (in light gray) ventricular chambers. On the right, tractographies of a few fibers that illustrates the fiber orientation (computed with MedINRIA, where coloring indicates the local fiber orientation).

Subject	Weight	Height	Age	Heart Weight (limit)	Sex	Septal thick.
1	60 Kg	158 cm	74	385 g (420 g)	F	12 mm
2	74 Kg	166 cm	47	385 g (444 g)	M	14 mm
3	102 Kg	192 cm	17	435 g (521 g)	M	10 mm
4	74 Kg	180 cm	47	430 g (444 g)	M	11 mm
5	77 Kg	165 cm	27	350 g (425 g)	F	11 mm
6	85 Kg	189 cm	21	365 g (473 g)	M	14 mm
7	63 Kg	175 cm	20	320 g (406 g)	M	12 mm
8	97 Kg	187 cm	21	410 g (506 g)	M	11 mm
9	77 Kg	179 cm	21	380 g (450 g)	M	12 mm
10	84 Kg	177 cm	50	460 g (473 g)	M	10 mm

TABLE I
CHARACTERISTICS OF THE HUMAN DATASET OF 10 HEALTHY HEARTS (SUBJECT WEIGHT, HEIGHT AND AGE, WITH MYOCARDIAL WEIGHT, MAX ALLOWED WEIGHT, AND SEPTAL THICKNESS.).

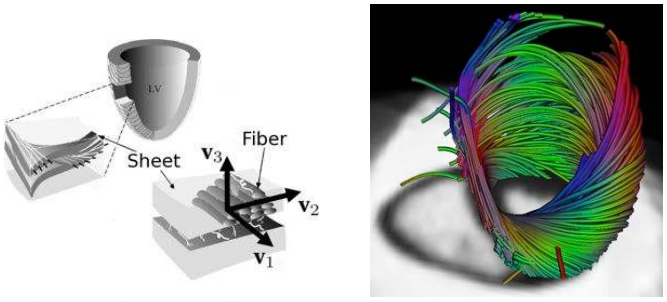

(a) Tensor eigenvectors with respect to the fiber and laminar sheet

(b) Atlas fiber tractography of the left ventricle and a short axis slice

Fig. 6. *Fiber architecture*: *(a)* Illustration of the Tensor eigenvectors, $\mathbf{v}_{1,2,3}$, with respect to the fiber and the laminar sheet (adapted from [28]). *(b)* The transmural variation of the fiber orientations in the left ventricle is visible in the fiber tractography (computed with MedINRIA) of the average tensor field.

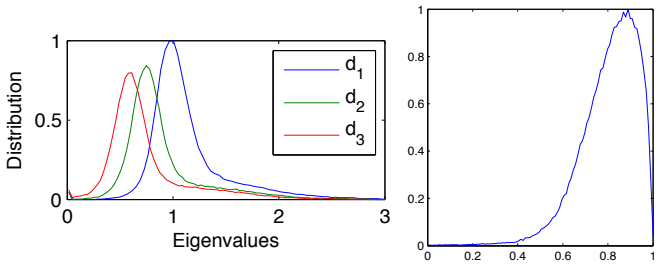

(a) Distribution of eigenvalues

(b) Transverse anisotropy

Fig. 7. *Transverse anisotropy*. *(a)* Distribution of the eigenvalues for all subjects. *(b)* Distribution of the ratio between the third and second eigenvalues, d_3/d_2, showing a transverse anisotropy for all subjects (i.e., the ratio peak at 0.86).

AHA segments of all hearts R-values with a significance level of 1% consistently well above $R_c = 0.06$ (away from the uniform distribution) which give another indication that the diffusion is transversely anisotropic, i.e., there is a secondary structure in the human fiber architecture.

B. Atlas Construction

The statistical atlas is constructed using four steps, illustrated in Fig. 1. First, the myocardium of each heart is segmented out on the $b = 0$ image of the DT-MRI acquisition. They are similar to T2-weighted images providing anatomical information with the advantage of being acquired and corrected for motion together with diffusion-weighted images (DWI) and thus aligned with the estimated DT-MRI. Information on the fiber architecture (i.e., any directional data such as DT-MRI or corresponding DWI) is purposely omitted from the registration process in order to avoid introducing any bias in the study of the fiber variability. Second, each myocardium is registered to a reference image using solely the b=0 images and the myocardium masks. Third, the reference image is deformed toward the morphological average of all hearts by repeating the second and this third step iteratively until convergence. Fourth, and last, the resulting deformation fields computed from the registration process are used to warp all tensor fields to the morphological atlas (Fig. 2).

AHA	R Value	AHA	R Value	AHA	R Value
1	0.18 (± 0.10)	7	0.24 (± 0.06)	13	0.25 (± 0.13)
2	0.21 (± 0.10)	8	0.19 (± 0.07)	14	0.18 (± 0.10)
3	0.23 (± 0.09)	9	0.21 (± 0.06)	15	0.23 (± 0.09)
4	0.21 (± 0.10)	10	0.18 (± 0.08)	16	0.22 (± 0.10)
5	0.18 (± 0.12)	11	0.20 (± 0.06)	17	0.23 (± 0.09)
6	0.24 (± 0.06)	12	0.19 (± 0.05)		

TABLE II
R VALUE, CONFIDENCE THAT THE ANGULAR DISTRIBUTION OF THE 2^{nd} EIGENVECTOR AROUND THE 1^{st} EIGENVECTOR IS NOT UNIFORM (I.E., TRANSVERSE ANISOTROPY). MEAN VALUE FOR EACH AHA SEGMENT WITH ITS STANDARD DEVIATION.

1) Myocardium Segmentation: Due to the noisy nature of the available images, the boundary between the myocardium and the surrounding gel can not be captured with a simple thresholding segmentation. This is in contrast with the canine dataset used in [22], [23], [21], [46], [38], [37], [38] where the myocardium was clearly outstanding from its background. A semi-automatic method has thus been designed with minimal user interaction in mind. The Graph Cut algorithm [5] has been chosen for its efficiency and ease of use. The following details are provided for reproducibility of the results. An underlying 3D graph is constructed from a 3D image and a global optimal solution partitions the graph into an *object* and a *background*. The graph edges between neighboring pixels, say p and q with intensities i_p and i_q, are weighted with $w_{p,q} = \exp(-(i_p - i_q)^2/2\sigma^2)$, where σ is a penalizing term (e.g., the standard deviation of intensity differences). By setting different weights on both directions, boundaries from dark objects to bright backgrounds (e.g., dark myocardium within bright gel) can be favored (or vice versa, for bright objects on dark backgrounds). A directional edge from a dark pixel p to a bright pixel q (i.e., $i_p < i_q$) is privileged when its weight is $w_{p\to q} = \lambda w_{p,q}$ with $\lambda < 1$, while $w_{q\to p} = w_{p,q}$ remains the same. Two special nodes are added in the graph, a source representing the *object* and a sink representing the *background*. The algorithm needs only a few *seed* points, connected to the two special nodes, in the *object* and in the *background*. The Graph Cut algorithm finds a global optimal cut separating the nodes connected to the source from those connected to the sink, thus segmenting the *object* from its *background*. Fast interactions are also possible to correct any missed segmentation. Further details are available in [5]. In our workflow, the user marks on any 3D slice of a b=0 image a few points in the left ventricular and in the right ventricular blood pools. From these marks, three automatic 3D binary segmentations are performed:

- *Finding the Heart*: A graph is constructed from the whole image and the heart, including the blood pool, is isolated from its background using the marked points as *object seeds* and using the points (found automatically) lying on a sphere surrounding the initial marked points (a sphere large enough to be outside the heart) as *background seeds*. A boundary from a dark object (the dark myocardium) to a bright object (bright gel) is privileged with $\lambda = 0.95$ when $i_p < i_q$.
- *Finding the Myocardium*: A smaller graph is constructed from the previous heart mask and the myocardium is outlined from the blood pool using the initial marked points as *background seeds* and using the voxels lying on the inner boundary of the heart mask as *object seeds*.

Here again, edges from dark to bright are privileged with $\lambda = 0.95$.

- *Differentiating the Ventricles*: A graph is constructed from the myocardium mask and the blood pool is partitioned into the left and the right sides using the initial marked points in the left and in the right ventricles as *object* and *background seeds*. As both ventricular fillings have similar intensities, directional edges are identical (i.e., $\lambda = 1$).

This strategy ensures a topologically valid myocardium mask. Indeed, the first two graph cuts correspond to the epicardium and the endocardium and isolate the myocardium with no unconnected pieces while guaranteeing a mask of at least one voxel thick. Holes are thus not possible across the myocardial wall which is really thin in the right ventricle. From the generated binary masks, a 3D segmented image is created with four labels: background, left and right ventricles, and myocardium. The labeled images are shown on Fig. 5.

2) Heart Registration: The pairwise registrations of N hearts, $\{I_i\}_{i=1,\dots,N}$, to a reference image, I_{ref}, give the diffeomorphic transformations, $\{\phi_{I_i \to I_{\text{ref}}}\}_{i=1,\dots,N}$, required for the warping of the tensor fields. Fig. 1 shows three hearts before and after registration. To obtain a better registration and a fast convergence, the registration is performed in three steps:

- *Ventricle Rigid Alignment*: First, the labeled images are reoriented by aligning the centers of mass of each ventricle. A block matching algorithm [34] refines this rigid registration.
- *Mask Non-rigid Registration*: Second, the aligned labeled images are transformed using a non-rigid registration [50], [32].
- $b = 0$ *Non-rigid Registration Refinement*: Third, and last, the previous transformation initializes the non-rigid registration of the masked $b=0$ images where only the myocardial regions are considered.

The pairwise registrations are performed with the Symmetric Log-domain Diffeomorphic Demons [50], [32]. In this extension of the Diffeomorphic Demons [51], the transformation ϕ is constrained to be in the one parameter subgroup of diffeomorphisms with stationary velocity field by parameterizing ϕ with the velocity field v, such that $\phi = \exp(v)$. Thus, the Log-domain Diffeomorphic Demons algorithm can be formulated as an alternate optimization scheme of the following energy with respect to the velocity fields v_c (hidden variable) and v:

$$E(I_{\text{ref}}, I_{\text{flo}}, v, v_c) = \frac{1}{\sigma_i^2} \parallel I_{\text{ref}} - I_{\text{flo}} \circ \exp(v_c) \parallel^2 + \frac{1}{\sigma_x^2} \parallel \log(exp(-v) \circ \exp(v_c) \parallel^2 + \frac{1}{\sigma_T^2} \parallel \nabla v \parallel^2,$$

where $\sigma_{i,x,T}$ are penalizing terms, I_{ref}, a reference image, I_{flo}, a floating image, v, the velocity field such that $I_{\text{flo}} \circ \exp(v) \equiv I_{\text{ref}}$, and the velocity field v_c, a hidden variable whose exponential is called the correspondence. The optimization of this energy is implemented in [51] with two consecutive smoothing steps which use two parameters. Both are widths of smoothing kernels, one for the smoothing of the update field, $\sigma_{K_{\text{fluid}}} = 1.4$, and has a fluid behavior, and the second is for the smoothing of the displacement field, $\sigma_{K_{\text{diff}}} = 1.0$, and has an elastic behavior.

Since the Demons algorithm is based on a sum of squared differences (SSD) and applied to MR images, whose intensities are not standardized, a histogram matching with the reference image is performed before each non-linear registration of b=0 images.

We use here the symmetric version of the Log-demons [50] where the registration is independent from the choice of the reference image, i.e., $\phi^{-1}_{I_{\text{flo}} \to I_{\text{ref}}} = \phi_{I_{\text{ref}} \to I_{\text{flo}}}$. The forward and backward velocity fields, $v_{I_{\text{flo}} \to I_{\text{ref}}}$ and $v_{I_{\text{ref}} \to I_{\text{flo}}}$, are computed independently as detailed previously and then averaged.

The Log-domain Diffeomorphic Demons has the advantage of providing stationary velocity fields that can be averaged or negated to respectively average and invert corresponding diffeomorphic transformations [2]. This property is particularly useful and efficient in the iterative steps of atlas construction detailed in the following subsection II-B3.

3) Construction of the Morphological Atlas: The construction of the atlas follows Guimond's *et al.* method [17] where the reference heart converges iteratively toward an average heart shape. In practice, only 5 iterations are required and the process is independent to the initial reference heart. At each iteration $(t+1)$, the reference heart from previous iteration (t), $I^{(t)}_{\text{ref}}$, is recomputed using the average of all inverse transforms, i.e., $I^{(t+1)}_{\text{ref}} = \frac{1}{N} \sum_{i=1}^{N} I_i \circ \phi_{I_i \to I^{(t)}_{\text{ref}}} \circ \phi_{I^{(t)}_{\text{ref}} \to I^{(t+1)}_{\text{ref}}}$ to converge to an average heart shape and intensities. The transformation updating the reference image is $\phi_{I^{(t)}_{\text{ref}} \to I^{(t+1)}_{\text{ref}}} = \exp\left(\frac{1}{N} \sum_{i=1}^{N} v_{I^{(t)}_{\text{ref}} \to I_i}\right)$. This can be computed in the Log-domain using the negated velocity fields: $v_{I^{(t)}_{\text{ref}} \to I_i} = -v_{I_i \to I^{(t)}_{\text{ref}}}$, where all $v_{I_i \to I^{(t)}_{\text{ref}}}$'s were previously computed during the pairwise registration of all hearts to the reference image, thus: $\phi_{I^{(t)}_{\text{ref}} \to I^{(t+1)}_{\text{ref}}} = \exp\left(-\frac{1}{N} \sum_{i=1}^{N} v_{I_i \to I^{(t)}_{\text{ref}}}\right)$. All steps and iterations of the atlas construction, the N pairwise registrations (times the number of iterations), are fully automated with no user interaction required. This is again in contrast with the method used in [38] which required numerous user interaction with manual landmarks positioning.

4) Tensor Warping: The original tensor fields, $\{\tilde{D}^{(i)}\}_{i=1,\dots,N}$, associated with each $b = 0$ image, are warped to the converged average heart shape using the final transformations $\{\phi_{I_i \to I_{\text{ref}}}\}_{i=1,\dots,N}$. Since diffusion tensors hold directional information, the warping of diffusion tensor fields includes a tensor reorientation step. Among two most common reorientation strategies [1], the Finite Strain strategy is preferred to the Preservation of the Principal Direction for its preservation of geometric features [38]. With the Finite Strain strategy, the reorientation of diffusion tensors is defined as the rotational component $R = (AA^t)^{-1/2}A$ of the local linear approximation $A = \nabla\phi^{-1}$ of the first derivative of the inverse transformation ϕ at each voxel. In the next sections, the warped tensor fields are referred as $\{D^{(i)}\}_{i=1,\dots,N}$ such that $D^{(i)} = R \cdot \tilde{D}^{(i)} \circ \phi_{I_i \to I_{\text{ref}}} \cdot R^t$.

C. Statistics on Tensor Fields

Statistics on diffusion tensor fields is not straightforward due to the nature of the diffusion tensor space. Indeed, the diffusion tensor space of symmetric positive definite matrices does not have a vector space structure with the standard Euclidean metric [26]. Among valid metrics proposed in the literature [36], the Log-Euclidean metric [3] is preferred for its simple and fast framework with a closed form solution. Usual statistics, such as the mean and the covariance, are thus computed with:

$$\overline{D} = \exp\left(\frac{1}{N}\sum_{i=1}^{N}\log(D^{(i)})\right) \quad (1)$$

$$\Sigma = \frac{1}{N-1}\sum_{i=1}^{N}\mathrm{vec}(\Delta D^{(i)})\cdot\mathrm{vec}(\Delta D^{(i)})^t, \quad (2)$$

where $\Delta D^{(i)} = \log(D^{(i)}) - \log(\overline{D})$ and $\mathrm{vec}(D) = (D_{11}, \sqrt{2}D_{12}, D_{22}, \sqrt{2}D_{31}, \sqrt{2}D_{32}, D_{33})^t$ is the condensed form of a diffusion tensor (redundant terms of the symmetric matrix $(D_{ij})_{i,j=1,2,3}$ are gathered). The mean diffusion tensor field, $\overline{D}$, is computed from N warped tensor fields $\{D^{(i)}\}_{i=1,\ldots,N}$.

Fig. 5 shows the tractography of a few fibers from six subjects. Fig. 6 (b) shows the tractography of the average diffusion tensor field. The variability of the diffusion tensors, for a particular voxel, is embedded in the covariance matrix, Σ.

The measure of the global variability can be assessed with the trace of the covariance matrix:

$$\sqrt{\mathrm{Trace}(\Sigma)} = \sqrt{\frac{1}{N-1}\sum_{i=1}^{N}\|\mathrm{vec}(\Delta D^{(i)})\|^2} \quad (3)$$

In the Log-space, $\Delta D^{(i)} = \log\left(D^{(i)}\right) - \log\left(\overline{D}\right)$ is equivalent to a ratio. The square root $\sqrt{\mathrm{Trace}(\Sigma)}$ expresses, therefore, a relative ratio of all diffusion tensors, $\{D^{(i)}\}_{i=1,\ldots,N}$, to the mean $\overline{D}$.

The measure of local variability of the cardiac fiber structures relies on the analysis of the eigenvectors of the mean diffusion tensor, $\mathbf{v}_{1,2,3}$ extracted from $\overline{D}$. The standard deviations of orientation differences, $\{\sigma_{\theta_{i,j}}\}_{i,j=1,2,3}$, between the coupled $(\mathbf{v}_i, \mathbf{v}_j)$ axes around $\mathbf{v}_k$ (i.e., the variability of how the orthogonal axes $(\mathbf{v}_i, \mathbf{v}_j)$ rotates around $\mathbf{v}_k$) are computed by projecting the covariance matrix Σ onto the orthonormal bases $\{W_{i,j}\}_{i,j=1,2,3}$:

$$\sigma_{\theta_{i,j}} = \arctan\left(\frac{1}{2(\lambda_i-\lambda_j)^2}[\mathrm{vec}(W_{i,j})^t\cdot\Sigma\cdot\mathrm{vec}(W_{i,j})]\right)^{\frac{1}{2}} \quad (4)$$

where $\lambda_{1,2,3}$ are the tensor eigenvalues in the Log-space, and the orthonormal bases are defined with:

$$W_{2,3} = \left(\mathbf{v_3}\cdot\mathbf{v_2}^t + \mathbf{v_2}\cdot\mathbf{v_3}^t\right)/\sqrt{2}$$
$$W_{1,3} = \left(\mathbf{v_3}\cdot\mathbf{v_1}^t + \mathbf{v_1}\cdot\mathbf{v_3}^t\right)/\sqrt{2}$$
$$W_{1,2} = \left(\mathbf{v_2}\cdot\mathbf{v_1}^t + \mathbf{v_1}\cdot\mathbf{v_2}^t\right)/\sqrt{2}.$$

The statistics are performed directly on tensors, i.e., eigendecomposition is only necessary on the average diffusion tensor field. There is thus no need to account for the sign ambiguity, which is inherent from the eigenvector extraction [4], when computing statistics.

The variability of the tensor eigenvalues measures the coherence of the diffusion along the three principal directions. The eigenvalues of all the tensors are expressed in the Log-space, $\{\lambda^{(i)}_{1,2,3}\}_{i=1,\ldots,N}$ such that $\lambda = \log(d)$ where d is the eigenvalue in the Euclidean-space. Their standard deviations σ_{λ_1}, σ_{λ_2}, and σ_{λ_3}, are the projections of the covariance matrix Σ onto the orthonormal bases $W_{1,1}$, $W_{2,2}$, and $W_{3,3}$:

$$\sigma_{\lambda_i} = \sqrt{\mathrm{vec}(W_i)^t\cdot\Sigma\cdot\mathrm{vec}(W_i)}, \quad (5)$$

where the orthonormal bases are defined with:

$$W_1 = \mathbf{v}_1\cdot\mathbf{v}_1^t$$
$$W_2 = \mathbf{v}_2\cdot\mathbf{v}_2^t$$
$$W_3 = \mathbf{v}_3\cdot\mathbf{v}_3^t.$$

In the Log-space, the standard deviation σ_λ is a ratio of all eigenvalues expressed in the Euclidean space, $\{d^{(i)}\}_{i=1,\ldots,N}$, relative to their mean $\overline{d}$.

III. Experimental Results

The statistical study of the human cardiac fiber architecture is presented here from a global point of view, showing the variability within a population of the whole diffusion tensor, to a more detailed approach, showing the variability of the principal directions of diffusion.

Due to many external factors, such as the temperature during acquisition (known to affect the diffusion values), the tensor fields have different scalings among all hearts. The histograms of the traces of the tensor matrices show significant disparities among a population. Therefore, before using them for statistical analysis, all acquired tensor fields, $\{\tilde{D}^{(i)}\}_{i=1,\ldots,N}$, are normalized using the modes of the histograms of the tensor traces for each patient. For the i^{th} patient:

$$\tilde{D}^{(i)} \leftarrow \tilde{D}^{(i)}\frac{\frac{1}{N}\sum_{j=1}^{N}\mathrm{mode}\left(\mathrm{Trace}(\tilde{D}^{(j)})\right)}{\mathrm{mode}\left(\mathrm{Trace}(\tilde{D}^{(i)})\right)}$$

The eigenvectors of the tensors fields remain unchanged with this normalization, and the eigenvalues are equally scaled in order to be able to compare all tensor fields on a common reference.

A. Fiber Variability

The global variability of the tensor field is measured with the square root of the trace of the covariance matrix (Eq. 3). Its histogram shows a peak of variability at 13.2% (Fig. 8(a,b)). It is important to note that this variability also includes acquisition and registration errors. While certain areas, such as around the apex, might show a higher variability due to a less organized fiber structure, other areas, such as the right ventricle, show an increased variability maybe due to registration errors. Indeed, large deformations in low resolution images make the registration challenging.

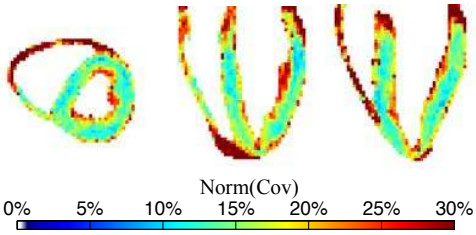

(a) Global variability of the whole tensor field

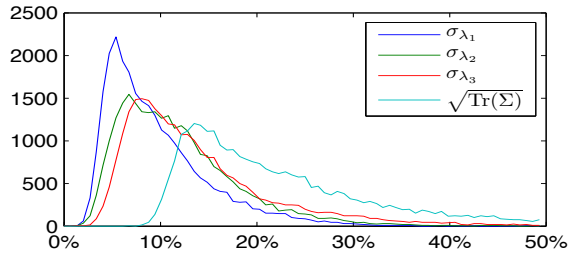

(b) Histogram of the eigenvalue variability and the global variability

Fig. 8. *Global variability*: (a) Variability of the eigenvalues in the statistical atlas of the tensor fields. The distribution of the primary eigenvalue standard deviations (expressed in percentage) of all hearts have a mode of $\sigma_{\lambda_1} = 5.35\%$ from the statistical mean. The second eigenvalues have a mode of $\sigma_{\lambda_2} = 6.35\%$. The tertiary eigenvalues have a mode of $\sigma_{\lambda_3} = 8.69\%$. (b) The histogram of the global variability ($\sqrt{\mathrm{Tr}(\Sigma)}$, Eq. 3) (expressed in percentage) of the whole diffusion tensor shows a mode of 13.2%.

The distributions of the standard deviations of the three eigenvalues are presented on Fig. 8(b). The primary eigenvalue is less variable than the two other eigenvalues. The mode of the standard deviations (Eq. 5) of the primary eigenvalue from the one of the statistical mean, expressed in percentage, is $\sigma_{\lambda_1} = 5.35\%$ compared to $\sigma_{\lambda_2} = 6.35\%$ and $\sigma_{\lambda_3} = 8.69\%$.

The orientation of the diffusion in human cardiac fibers has a different variability in each principal direction. The variability around $\mathbf{v}_1$, $\mathbf{v}_2$, and $\mathbf{v}_3$, is measured with the rotation of the tensor transverse $(\mathbf{v}_2, \mathbf{v}_3)$, longitudinal $(\mathbf{v}_1, \mathbf{v}_3)$, and equatorial $(\mathbf{v}_1, \mathbf{v}_2)$ planes around their normals. The standard deviations are formulated by Eq. 4. These angular variabilities are presented in Fig. 9. The dispersion of the fiber orientation, $\mathbf{v}_1$, has a standard deviation of rotation in the tensor longitudinal plane with a mode of $\sigma_{\theta_{1,3}} = 11.5°$, and in the tensor equatorial plane, $\sigma_{\theta_{1,2}} = 13.0°$. The variability of the laminar sheet orientation is described with the rotation of the tensor transverse plane around the fiber. Its standard deviation is $\sigma_{\theta_{2,3}} = 31.1°$. The laminar sheet structure is, thus, in humans, much more variable than the fiber structure. This concurs with previous canine studies [22], [23], [38], [15] where the fiber orientation (with $\sigma_{\theta_{1,3}} = 7.9°$ and $\sigma_{\theta_{1,2}} = 7.7°$) is more stable than the laminar sheet orientation (with $\sigma_{\theta_{2,3}} = 22.7°$).

B. Transmural Distribution

The variability of the fiber orientation is also analyzed by measuring the distribution of the helix angle (vertical angle, or helical pitch, of the fiber, Fig. 10(a)) and the transverse angle (horizontal angle of the fiber, Fig. 10(b)) along the transmural depth. These angles are defined to range from $-90°$ to $+90°$. For instance, an helix angle of $-90°$ is a fiber pointing toward the base of the heart, an helix angle of $+90°$ is a fiber pointing toward the apex, and a transverse angle of $-90°$ is a fiber pointing toward the ventricular cavity, a transverse angle of $+90°$ is a fiber pointing outward the ventricular cavity.

(i.e., fiber pointing toward the base of the heart) to $+90°$ (i.e., fiber pointing toward the apex). A prolate ellipsoidal model of the heart [33] is fitted to the morphology of the statistical atlas. The transmural variation of the fiber orientation is, thus, easier to measure with the mapped prolate ellipsoidal coordinates. The distributions are presented in a joint histogram (Fig. 10(c,d)) where the angle distribution, on the vertical axis, is plotted against all transmural distances, on the horizontal axis.

The helix angle varies globally from $-41°(\pm 26°)$ (plus or minus its standard deviation) on the epicardium to $+66°(\pm 15°)$ on the endocardium. The mode of the helix angle is $-48°$ on the epicardium and $+64°$ on the endocardium. The range of the helix angle in humans, $107°$, concurs with the results of a canine study [37] that showed a range of $110°$. It appears to be consistent across the myocardium, as seen on Fig. 11, only the apex presents a drastic difference. The helix angle is strongly correlated to the transmural distance with a correlation factor of $\rho = 0.831$, i.e., this suggests a linear dependence between the helix angle and the transmural location. This correlation also concurs with the findings of the histological study [16] of *postmortem* human hearts. Their sparse distribution of helix angles varies from about $-40°$ on the epicardium to about $+40°$ on the endocardium. The main difference between our results and the ones in [16] (human data) and [37] (canine data) is the absence of inflection points in the shape of the helix angle distribution. This might be due to the low resolution of our dataset. On the other hand, the transverse angle is less correlated with $\rho = 0.286$, i.e., it depends less on the fiber location. The average transverse angles suggest indeed that the fibers are relatively parallel to the epicardium with an average angle of $+7°(\pm 31°)$. The angles appear to be more stable in the midwall with an average transverse angle of $+9°(\pm 12°)$. The transverse angles are higher on the endocardium with $+34°(\pm 29°)$.

The delineation of the myocardium into 17 AHA segments (by the American Heart Association [7]) in the left ventricle gives more details in each of these regions. The angular variability is summarized in Fig. 11. The correlation factor of the helix angle appears to be high across all myocardial segments. The apex (segment 17), however, shows a low correlation factor of $\rho = 0.355$. A canine study [37] showed similar results with a coherent helix angle, also with small dissimilarities across the segments.

IV. Limitations

The statistical analysis brings out a challenging task, still unsolved: distinguishing the true variability of the fiber structure from errors due to acquisition and registration. The statistical analysis is likely to suffer from several limitations. Starting with the imaging of the cardiac fibers, the choice of the acquisition protocol affects the image resolution and noise. It was shown in [14] that among a panel of acquisition

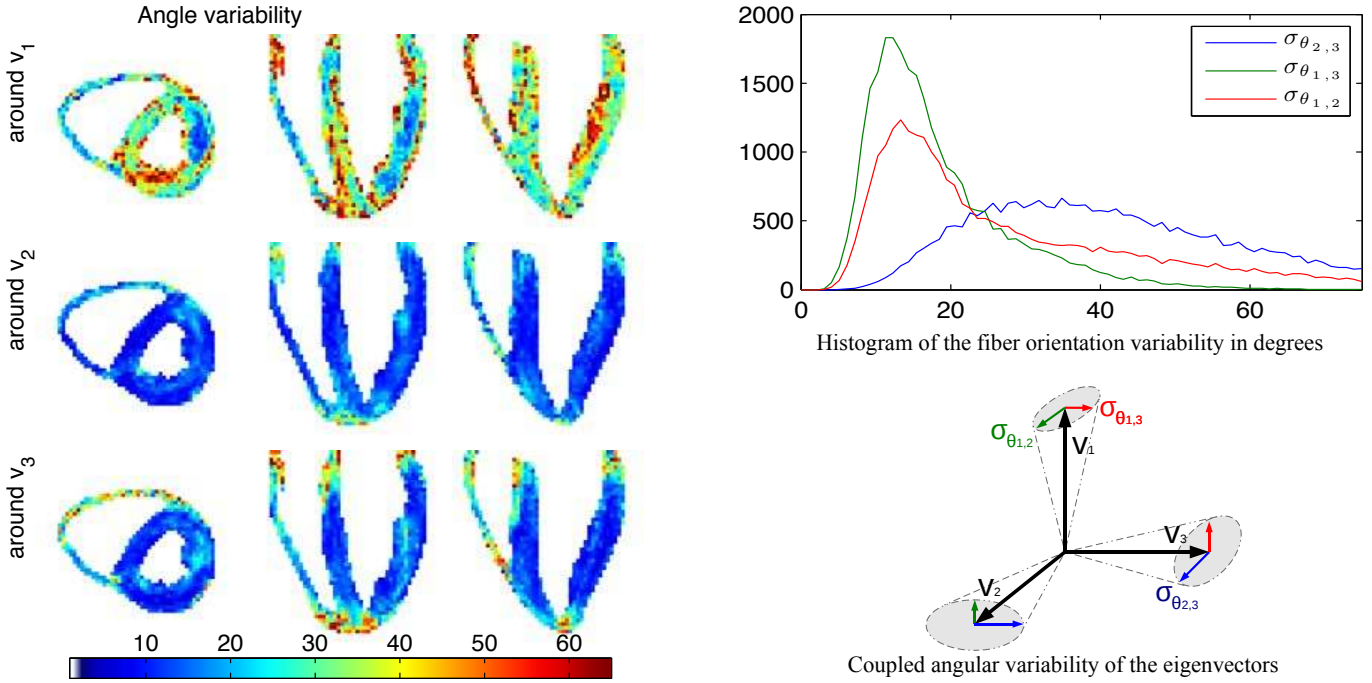

Fig. 9. Standard deviation of the fiber orientation (expressed in degree). *Top row of the images and in the blue histogram*: Variability of the laminar sheet orientation, $\sigma_{\theta_{2,3}}$ around $\mathbf{v}_1$, with a mode at $31.1°$. *Middle row and in the green histogram*: Variability of the fiber orientation, $\sigma_{\theta_{1,3}}$ around $\mathbf{v}_2$, with a mode at $11.5°$. *Bottom row and in the red histogram*: Variability of the fiber orientation, $\sigma_{\theta_{1,2}}$ around $\mathbf{v}_3$, with a mode at $13.0°$.

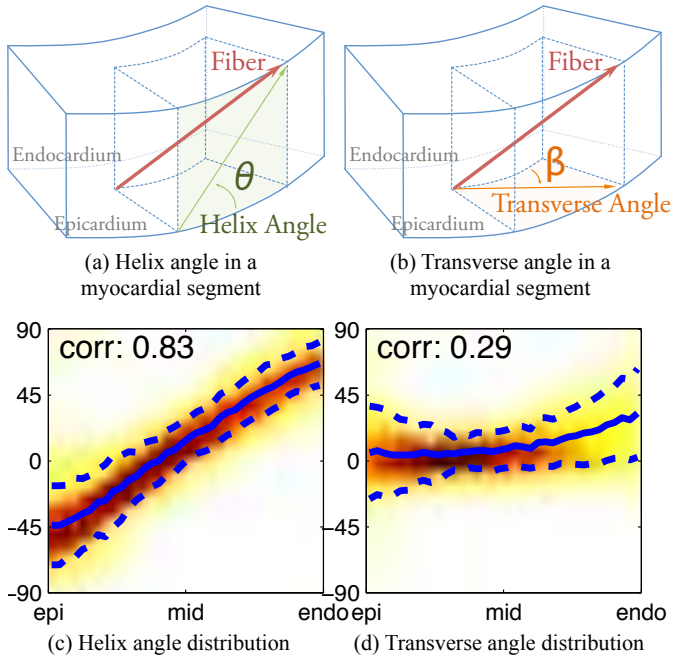

(a) Helix angle in a myocardial segment

(b) Transverse angle in a myocardial segment

(c) Helix angle distribution

(d) Transverse angle distribution

Fig. 10. *Transmural variability*: *(a)* Illustration of the helix angle in a myocardial segment (angle on the tangent plane of the epicardium, in green), *(b)* of the transverse angle (angle on the horizontal normal plane, in orange), *(c)* joint histogram showing the distribution of the helix angle, varying from $-41°$ to $+66°$, and *(d)* the transverse angle, which shows fibers more parallel to the epicardium. The x axis is the transmural distance from epicardium *(left)* to endocardium *(right)*. The y axis is the helix or transverse angle. The color is the probability distribution of an angle for a particular transmural distance. The thick blues lines are the average angles across the wall, and the dashed lines are the one-standard-deviation envelope. The correlation factor between the angle and the transmural distance is given.

protocols applied specifically to human heart *ex vivo* DWI with a comparison of different sets of directions and repetitions, the use of 12 directions with 4 repetitions gives for *ex vivo* the best results in terms of fiber direction coherence, while only 6 directions are preferred in [19]. Using 48 unique directions might for instance provide a better angular resolution in addition to a better signal to noise ratio. The imaging protocol described in [12], [13] shows that the peak signal-to-noise ratio during acquisition of the dataset is 16.44 dB. The variability due to acquisition can be assessed more precisely by imaging several times the same heart, or with bootstrapping resampling methods [25], [20], [35] when the number of acquisitions is limited. Our results include these inherent uncertainties and can be further refined with more precise acquisition schemes. The variability study can also be limited by a partial volume effect which is enhanced in the presence of larger voxel sizes. For instance, the myocardium in our dataset (which has a resolution of 2mm^3) appears as 6 or 7 voxel wide. The spatial resolution was mostly limited due to time constraints. Indeed, the hearts had to be imaged soon after death within a limited amount of time before being given back for autopsy in its original state. Additionally, the lack of fixative or any solutions to prevent contracture may have influenced the fiber architecture. Nonetheless, our framework is independent of the acquisition protocol and our results can be refined in the future with any improved diffusion tensor imaging protocol.

The method used to construct the atlas also has limitations. For instance, the segmentation of the myocardium has not been designed to remove the few voxels representing the fat lying on the myocardium. This is for instance observed in subject 1 (Fig. 5) where darker voxels surrounds part of

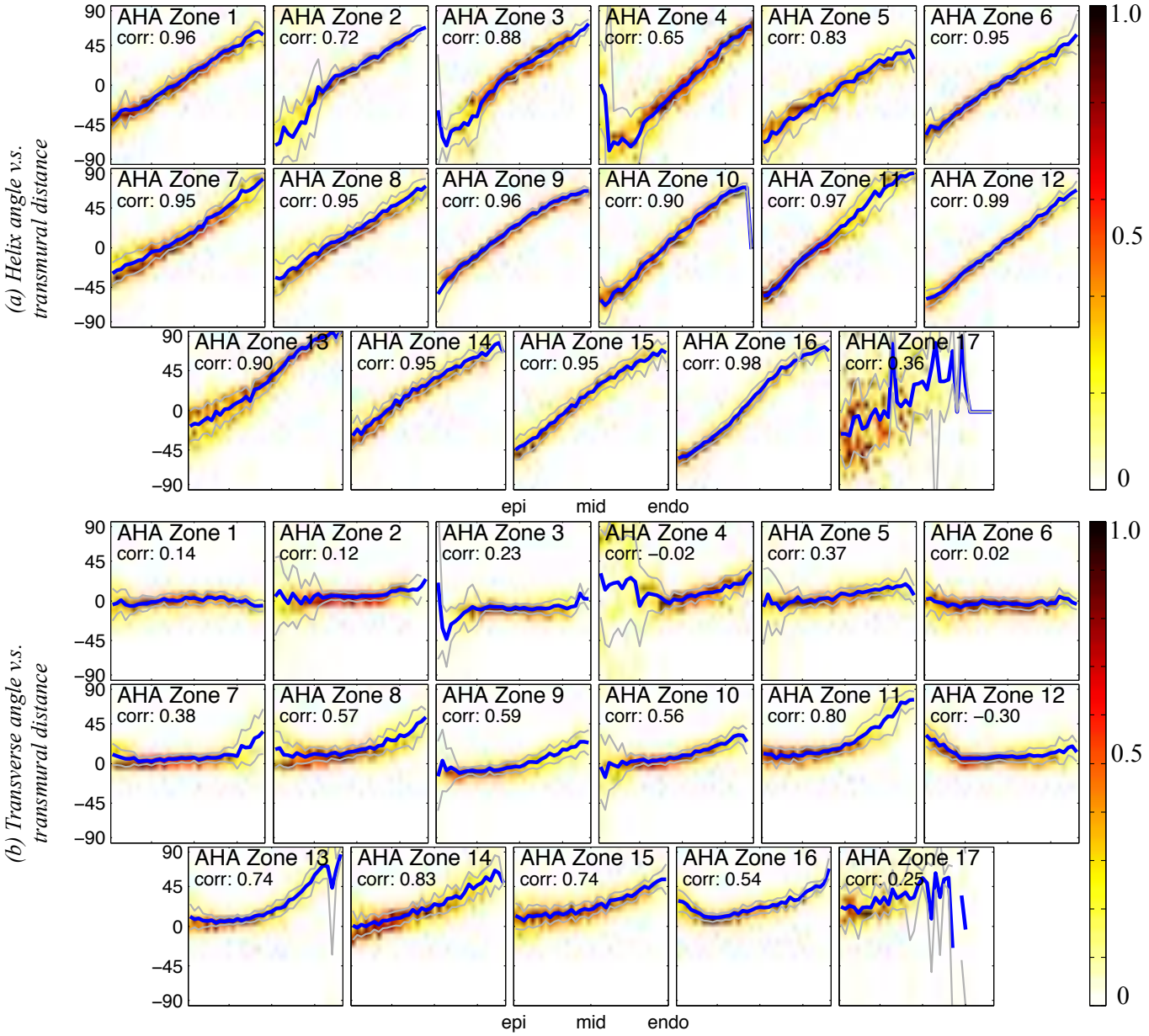

Fig. 11. Joint histograms showing the distribution along the transmural depth of *(a)* the helix angle and *(b)* the transverse angle of the human cardiac fibers, from the epicardium (*left side of histogram*) to the endocardium (*right side of histogram*), in the 17 AHA segments of the left ventricle. The thick blue lines are the average angles across the wall, and the light gray lines are the one-standard-deviation envelope. The correlation factor between the angle and the transmural distance is given for each segment.

the myocardium. Another limitation comes from the large variability in the heart shapes among a population, which makes the registration a challenging step with the presence of large deformations. This is for example particularly true in the right ventricular and apical regions. The Diffeomorphic Demons, guaranteeing smooth direct and inverse deformation fields, were chosen for this reason. Although no ground truth is available to assess the registration accuracy, the Dice metrics between the myocardium masks of all subjects and the atlas (defined as the ratio of intersection to addition set: $2\left(|S| \cap |T|\right) / \left(|S| + |T|\right)$, with $|S|$ and $|T|$ being mask volumes), which range from 0.86 to 0.88, can provide a certain confidence that there is a good boundary overlap between all registered hearts and the atlas. Moreover, the statistical study is currently limited [54] by the number of available hearts. Since human hearts classified as *healthy* are extremely difficult to obtain, we chose to use the maximal number of hearts available to us. Our analysis on the variability of the fiber architecture is thus limited by the inherent errors due to acquisition and registration.

V. Discussion and Conclusion

The work reported in this paper provides the first statistical atlas of the human cardiac fiber architecture that enabled a quantitative analysis of the fiber variability among a healthy population. The statistical atlas has been constructed from 10

ex vivo hearts with a method minimizing user interaction. The hearts were non-rigidly registered by purposely omitting any micro structure information (e.g., fiber orientations) in order to avoid a bias in the statistical study of the fiber architecture (e.g., similarly to studying the variability of fingerprint lines, we would not include information on these line orientations, as this is exactly what we want to measure; we want to see how variable the line orientations are in different regions and across a population; registering directly these fingerprint lines would in fact remove, or lessen, any variability in their orientations). The transmural walls were all registered in a similar manner, all based on the myocardium shapes. The spatial variability of the fiber architecture were thus preserved in the registered tensor fields. The deformation fields, obtained while constructing the morphological atlas of the heart, were used to warp all tensor fields, with the finite strain reorientation strategy, to the atlas reference. Another approach would have been to warp directly the diffusion-weighted images and reestimate the diffusion tensor. This approach would have required a strategy for the local deformation of the gradient orientations which is also not necessarily trivial. A mean tensor field was computed using the Log-Euclidean metric. The variability of the mean tensor field is expressed in a covariance matrix. Global statistics on the whole diffusion tensor highlights myocardial regions of high variability. The diffusion tensors in the compact left ventricular myocardium remain stable with a global variability of 13.2%. The statistical framework provides means to study the variability of the eigenvectors in specific directions, where, the fibers are shown to vary with $\pm 11.5^\circ$ in the $\mathbf{v}_{1,3}$ plane and with $\pm 13.0^\circ$ in the $\mathbf{v}_{1,2}$ plane. Their variability is coherent across the whole myocardium. The secondary and tertiary eigenvectors, assumed to be associated with the laminar sheet normal, are, however, less stable compared to the fiber structure with a variability of $\pm 31.1^\circ$. This concurs with a previous canine study [38]. Such high variability either shows that the laminar sheet structure is less organized than the fiber structure (e.g. the presence of two populations of orthogonal laminar sheets randomly distributed over a given heart [21], [31]), or not be present everywhere. Additionally, the distribution of the actual angular values of the fiber orientation has been studied across several myocardial segments. The helix angle spans from $-41^\circ(\pm 26^\circ)$ on the epicardium to $+66^\circ(\pm 15^\circ)$ on the endocardium. The angular transmural distribution shows an helix angle highly correlated with the transmural depth. The histological study of *postmortem* human hearts [16] similarly observe a transmural correlation of the helix angle. Differences in the shape and in the variance of the helix angle distribution between our results and the ones in [16], [38] might be due to our coarser resolution. The average transverse angle shows that the cardiac fibers are relatively parallel to the myocardium epicardium. The small deviations from the average transverse angle might also be due to an underlying spiral architecture of the fibers, where fibers tracked initially on the epicardium create a spiral around the ventricle and find themselves at last to be on the endocardium. This change might occur in the apical sections where the deviations from zero are more apparent than in the basal sections.

The statistical study of the fiber architecture which plays a key role in mechanical and electrical cardiac functions, gives a better understanding of the human heart by providing the spatial distribution of fiber angles with their variations. These numbers will eventually be refined with the availability of more *ex vivo* human hearts and with DT-MRI acquisitions at higher resolutions. Moreover, the computation of the statistical atlas is simplified with the developed semi-automatic method. The human statistical atlas will thus be easily refined with future acquisitions of healthy hearts. Larger multi-population studies involving many hearts will likewise benefit from our method. For instance, cardiac pathologies could be characterized by comparing the fiber architecture against this atlas of healthy hearts [30]. A more appropriate comprehension of the human cardiac fiber architecture is also relevant to the creation of more elaborate computational models that could for instance be used for the planning of radiofrequency ablation (RFA) and cardiac resynchronization therapy (CRT), or to fiber-based surgical treatments [8], [9], which offer a promising perspective to the restoration of failing ventricles. The use of this human statistical atlas could also ideally improve the diagnosis and the follow-up of cardiac diseases related to fiber structural defects. With ongoing research in *in vivo* DT-MRI or in Shear Wave Imaging [27], extrapolation of sparse *in vivo* acquisitions with an accurate human atlas could pave the way for more personalized *in vivo* imaging [48] and cardiac modeling.

Acknowledgement

The authors wish to acknowledge helpful comments from Leon Axel, constructive discussions with Xavier Pennec, Maxime Sermesant and Marco Lorenzi from the Asclepios Team, as well as the anonymous reviewers for their valuable comments and suggestions.

References

[1] D. C. Alexander, C. Pierpaoli, P. J. Basser, and J. C. Gee. Spatial transformations of diffusion tensor magnetic resonance images. *IEEE Transactions on Medical Imaging*, 20(11):1131–1139, 2001.[1441]

[2] V. Arsigny, O. Commowick, X. Pennec, and N. Ayache. A Log-Euclidean framework for statistics on diffeomorphisms. In *MICCAI*, pages 924–931, 2006.[1441]

[3] V. Arsigny, P. Fillard, X. Pennec, and N. Ayache. Log-Euclidean metrics for fast and simple calculus on diffusion tensors. *Magnetic Resonance in Medicine*, 56(2):411–421, 2006.[1442]

[4] P. J. Basser and S. Pajevic. Statistical artifacts in diffusion tensor MRI (DT-MRI) caused by background noise. *Magnetic Resonance in Medicine*, 44(1):41–50, 2000.[1442]

[5] Y. Boykov and M.-P. Jolly. Interactive organ segmentation using graph cuts. In *MICCAI*, pages 276–286, 2000.[1437, 1440]

[6] J. D. Bronzino. *Biomedical Engineering Handbook*, volume 1. Springer-Verlag Berlin and Heidelberg, 1995.[1436]

[7] M. Cerqueira, N. Weissman, V. Dilsizian, A. Jacobs, S. Kaul, W. Laskey, D. Pennell, J. Rumberger, T. Ryan, and M. Verani. Standardized myocardial segmentation and nomenclature for tomographic imaging of the heart: a statement for healthcare professionals from the cardiac imaging committee of the council on clinical cardiology of the American Heart Association. *Circulation*, 105(4):539–542, 2002.[1443]

[8] M. Cirillo. A new surgical ventricular restoration technique to reset residual myocardium's fiber orientation: the "KISS" procedure. *Annals of Surgical Innovation and Research*, 3, 2009.[1436, 1446]

[9] M. Cirillo, M. Campana, F. Brunelli, M. D. D. Tomba, Z. Mhagna, A. Messina, E. Villa, and G. Troise. 'let's twist again': surgically induced renewal of left ventricular torsion in ischemic cardiomyopathy. *Journal of Cardiovascular Medicine*, 11(1):34–39, 2010.[1436, 1446]

[10] K. D. Costa, J. W. Holmes, and A. D. Mcculloch. Modelling cardiac mechanical properties in three dimensions. *Mathematical, Physical and Engineering Sciences*, 359(1783):1233–1250, 2001.[1436]

[11] P. Fillard, C. Poupon, and J. F. Mangin. A novel global tractography algorithm based on an adaptive spin glass model. In *MICCAI*, pages 927–934, 2009.[1438]

[12] C. Frindel. *Imagerie par résonance magnétique du tenseur de diffusion (IRM-TD) en imagerie cardiaque humaine : traitements et premières interprétations*. PhD thesis, Institut National des Sciences Appliquées de Lyon, 2009.[1436, 1438, 1444]

[13] C. Frindel, M. Robini, P. Croisille, and Y.-M. M. Zhu. Comparison of regularization methods for human cardiac diffusion tensor MRI. *Medical Image Analysis*, 13(3):405–418, 2009.[1436, 1438, 1444]

[14] C. Frindel, M. Robini, S. Rapacchi, E. Stephant, Y.-M. M. Zhu, and P. Croisille. Towards in vivo diffusion tensor MRI on human heart using edge-preserving regularization. *IEEE Engineering in Medicine and Biology Society*, pages 6008–6011, 2007.[1443]

[15] S. Gilbert, A. Benson, P. Li, and A. Holden. Visualisation of dog myocardial structure from diffusion tensor magnetic resonance imaging: the paradox of uniformity and variability. In *Functional Imaging and Modeling of the Heart*, pages 403–412, 2007.[1443]

[16] R. A. Greenbaum, S. Y. Ho, D. G. Gibson, A. E. Becker, and R. H. Anderson. Left ventricular fibre architecture in man. *British Heart Journal*, 45(3):248–263, 1981.[1436, 1443, 1446]

[17] A. Guimond, J. Meunier, and J. P. Thirion. Average brain models: a convergence study. *Computer Vision and Image Understanding*, pages 192–210, 2000.[1441]

[18] W. Harvey. *Exercitatio anatomica de motu cordis et sanguinis in animalibus*. 1628.[1436]

[19] K. M. Hasan, D. L. Parker, and A. L. Alexander. Comparison of gradient encoding schemes for diffusion-tensor MRI. *Magnetic Resonance Imaging*, 13(5):769–780, 2001.[1444]

[20] K. M. Hasan, D. L. Parker, and A. L. Alexander. Magnetic resonance water self-diffusion tensor encoding optimization methods for full brain acquisition. *Image Analysis and Stereology*, 21(2):87–96, 2992.[1444]

[21] P. A. Helm. *A novel technique for quantifying variability of cardiac anatomy: Application to the dyssynchronous failing heart*. PhD thesis, Johns Hopkins University, 2005.[1438, 1440, 1446]

[22] P. A. Helm, M. F. Beg, M. I. Miller, and R. L. Winslow. Measuring and mapping cardiac fiber and laminar architecture using diffusion tensor MR imaging. *Annals of the New York Academy of Sciences*, 1047:296–307, 2005.[1438, 1440, 1443]

[23] P. A. Helm, H.-J. J. Tseng, L. Younes, E. R. McVeigh, and R. L. Winslow. Ex vivo 3D diffusion tensor imaging and quantification of cardiac laminar structure. *Magnetic Resonance in Medicine*, 54(4):850–859, 2005.[1438, 1440, 1443]

[24] D. A. Hooks, K. A. Tomlinson, S. G. Marsden, I. J. LeGrice, B. H. Smaill, A. J. Pullan, and P. J. Hunter. Cardiac microstructure: implications for electrical propagation and defibrillation in the heart. *Circulation Research*, 91(4):331–338, 2002.[1436]

[25] D. K. Jones. Tractography gone wild: Probabilistic fibre tracking using the wild bootstrap with diffusion tensor MRI. *IEEE Transactions on Medical Imaging*, 27(9):1268–1274, 2008.[1444]

[26] D. K. Jones, L. D. Griffin, D. C. Alexander, M. Catani, M. A. Horsfield, R. Howard, and S. C. R. Williams. Spatial normalization and averaging of diffusion tensor MRI data sets. *NeuroImage*, 17(2):592–617, 2002.[1442]

[27] W. N. Lee, M. Pernot, M. Couade, E. Messas, P. Bruneval, A. Bel, A. A. Hagege, M. Fink, and M. Tanter. Mapping myocardial fiber orientation using Echocardiography-Based shear wave imaging. *IEEE Transactions on Medical Imaging*, 31(3):554–562, 2012.[1446]

[28] I. J. LeGrice, B. H. Smaill, L. Z. Chai, S. G. Edgar, J. B. Gavin, and P. J. Hunter. Laminar structure of the heart: ventricular myocyte arrangement and connective tissue architecture in the dog. *The American journal of physiology*, 269(2), 1995.[1436, 1440]

[29] H. Lombaert, J.-M. Peyrat, P. Croisille, S. Rapacchi, L. Fanton, P. Clarysse, H. Delingette, and N. Ayache. Statistical analysis of the human cardiac fiber architecture from DT-MRI. In *Functional Imaging and Modeling of the Heart*, volume 6666, pages 171–179, 2011.[1436]

[30] H. Lombaert, J.-M. Peyrat, L. Fanton, F. Cheriet, H. Delingette, N. Ayache, P. Clarysse, I. Magnin, and P. Croisille. Statistical atlas of human cardiac fibers: Comparison with abnormal hearts. In *Proceedings of STACOM Workshop at MICCAI*, pages 207–213, 2011.[1446]

[31] H. Lombaert, J.-M. Peyrat, L. Fanton, F. Cheriet, H. Delingette, N. Ayache, P. Clarysse, I. Magnin, and P. Croisille. Variability of the human cardiac laminar structure. In *Proceedings of STACOM Workshop at MICCAI*, pages 160–167, 2011.[1446]

[32] T. Mansi, X. Pennec, M. Sermesant, H. Delingette, and N. Ayache. iLogDemons: A Demons-Based registration algorithm for tracking incompressible elastic biological tissues. *International Journal of Computer Vision*, pages 1–20, 2010.[1437, 1441]

[33] P. M. Nielsen, I. J. Le Grice, B. H. Smaill, and P. J. Hunter. Mathematical model of geometry and fibrous structure of the heart. *American Journal of Physiology, Heart Circulatory Physiology*, 260(4):1365–1378, 1991.[1436, 1443]

[34] S. Ourselin, A. Roche, S. Prima, and N. Ayache. Block matching: a general framework to improve robustness of rigid registration of medical images. In *MICCAI*, pages 557–566, 2000.[1441]

[35] S. Pajevic and P. J. Basser. Parametric and non-parametric statistical analysis of DT-MRI data. *Journal of Magnetic Resonance*, 161(1):1–14, 2003.[1444]

[36] X. Pennec, P. Fillard, and N. Ayache. A Riemannian framework for tensor computing. *International Journal of Computer Vision*, 66(1):41–66, 2006.[1442]

[37] J.-M. Peyrat. *Comparison of cardiac anatomy and function: statistics on fibre architecture from DT-MRI and registration of 4D CT Images*. PhD thesis, Nice Sophia Antipolis University, 2009.[1440, 1443]

[38] J.-M. Peyrat, M. Sermesant, X. Pennec, H. Delingette, C. Xu, E. R. McVeigh, and N. Ayache. A computational framework for the statistical analysis of cardiac diffusion tensors: application to a small database of canine hearts. *IEEE Transactions on Medical Imaging*, 26(11):1500–1514, 2007.[1437, 1440, 1441, 1443, 1446]

[39] S. Rapacchi, P. Croisille, V. Pai, D. Grenier, M. Viallon, P. Kellman, N. Mewton, and H. Wen. Reducing motion sensitivity in free breathing DWI of the heart with localized Principal Component Analysis. In *International Society for Magnetic Resonance in Medicine*, 2010.[1436]

[40] J. Relan, P. Chinchapatnam, M. Sermesant, K. Rhode, M. Ginks, H. Delingette, C. Aldo Rinaldi, R. Razavi, and N. Ayache. Coupled personalization of cardiac electrophysiology models for prediction of ischaemic ventricular tachycardia. *Journal of the Royal Society Interface Focus*, 1(3):396–407, 2011.[1436]

[41] D. Rohmer, A. Sitek, and G. T. Gullberg. Reconstruction and visualization of fiber and laminar structure in the normal human heart from ex vivo diffusion tensor magnetic resonance imaging (DTMRI) data. *Investigative Radiology*, 42(11):777–789, 2007.[1436]

[42] D. F. Scollan, A. Holmes, J. Zhang, and R. L. Winslow. Reconstruction of cardiac ventricular geometry and fiber orientation using magnetic resonance imaging. *Annals of biomedical engineering*, 28(8):934–944, 2000.[1438]

[43] G. Seemann, D. U. J. Keller, D. L. Weiss, and O. Dossel. Modeling human ventricular geometry and fiber orientation based on diffusion tensor MRI. In *Computers in Cardiology*, pages 801–804, 2006.[1436]

[44] M. Sermesant, R. Chabiniok, P. Chinchapatnam, T. Mansi, F. Billet, P. Moireau, J. M. Peyrat, K. Wong, J. Relan, K. Rhode, M. Ginks, P. Lambiase, H. Delingette, M. Sorine, C. A. Rinaldi, D. Chapelle, R. Razavi, and N. Ayache. Patient-specific electromechanical models of the heart for the prediction of pacing acute effects in CRT: A preliminary clinical validation. *Medical Image Analysis*, 2011.[1436]

[45] D. D. Streeter, H. M. Spotnitz, D. P. Patel, J. Ross, and E. H. Sonnenblick. Fiber orientation in the canine left ventricle during diastole and systole. *Circulatory Research*, 24(3):339–347, 1969.[1436]

[46] H. Sundar, Dinggang Shen, G. Biros, H. Litt, and C. Davatzikos. Estimating myocardial fiber orientations by template warping. In *International Symposium on Biomedical Imaging*, pages 73–76, 2006.[1440]

[47] F. Torrent-Guasp, M. J. Kocica, A. F. Corno, M. Komeda, F. Carreras-Costa, A. Flotats, J. Cosin-Aguillar, and H. Wen. Towards new understanding of the heart structure and function. *European Journal of Cardio-Thoracic Surgery*, 27(2):191–201, 2005.[1436]

[48] N. Toussaint, M. Sermesant, C. T. Stoeck, S. Kozerke, and P. G. Batchelor. In vivo human 3D cardiac fibre architecture: reconstruction using curvilinear interpolation of diffusion tensor images. In *MICCAI*, pages 418–425, 2010.[1446]

[49] W.-Y. Y. Tseng, V. J. Wedeen, T. G. Reese, R. N. Smith, and E. F. Halpern. Diffusion tensor MRI of myocardial fibers and sheets: correspondence with visible cut-face texture. *Journal of Magnetic Resonance Imaging*, 17(1):31–42, 2003.[1438]

[50] T. Vercauteren, X. Pennec, A. Perchant, and N. Ayache. Symmetric log-domain diffeomorphic registration: a demons-based approach. In *MICCAI*, pages 754–761, 2008.[1437, 1441]

[51] T. Vercauteren, X. Pennec, A. Perchant, and N. Ayache. Diffeomorphic demons: efficient non-parametric image registration. *NeuroImage*, 45(1):S61–S72, March 2009.[1441]

[52] L. K. von Segesser. The myocardial band: fiction or fact? *European Journal of Cardio-Thoracic Surgery*, 27(2):181–182, 2005.[1436]

[53] M.-T. Wu, W.-Y. I. Tseng, M.-Y. M. Su, C.-P. Liu, K.-R. Chiou, V. J. Wedeen, T. G. Reese, and C.-F. Yang. Diffusion tensor magnetic resonance imaging mapping the fiber architecture remodeling in human myocardium after infarction: correlation with viability and wall motion. *Circulation*, 114(10):1036–1045, 2006.[1436]

[54] I. Young. Further consideration of sample and feature size (corresp.). *IEEE Transactions on Information Theory*, 24(6):773–775, 1978.[1445]

[55] L. Zhukov and A. H. Barr. Heart-muscle fiber reconstruction from diffusion tensor MRI. In *Visualization*, pages 597–602, 2003.[1436]